J Neurophysiol 119: 290–304, 2018.
First published October 18, 2017; doi:10.1152/jn.00447.2017.

RESEARCH ARTICLE | *Neural Circuits*

Intrinsic physiology of inhibitory neurons changes over auditory development

Briana J. Carroll,[1,4] Richard Bertram,[2,3,4] and Richard L. Hyson[1,4]

[1]*Department of Psychology, Florida State University, Tallahassee, Florida;* [2]*Deparment of Mathematics, Florida State University, Tallahassee, Florida;* [3]*Program in Molecular Biophysics, Florida State University, Tallahassee, Florida; and* [4]*Program in Neuroscience, Florida State University, Tallahassee, Florida*

Submitted 16 June 2017; accepted in final form 13 October 2017

Carroll BJ, Bertram R, Hyson RL. Intrinsic physiology of inhibitory neurons changes over auditory development. *J Neurophysiol* 119: 290–304, 2018. First published October 18, 2017; doi:10.1152/jn.00447.2017.—During auditory development, changes in membrane properties promote the ability of excitatory neurons in the brain stem to code aspects of sound, including the level and timing of a stimulus. Some of these changes coincide with hearing onset, suggesting that sound-driven neural activity produces developmental plasticity of ion channel expression. While it is known that the coding properties of excitatory neurons are modulated by inhibition in the mature system, it is unknown whether there are also developmental changes in the membrane properties of brain stem inhibitory neurons. We investigated the primary source of inhibition in the avian auditory brain stem, the superior olivary nucleus (SON). The present studies test the hypothesis that, as in excitatory neurons, the membrane properties of these inhibitory neurons change after hearing onset. We examined SON neurons at different stages of auditory development: embryonic days 14–16 (E14–E16), a time at which cochlear ganglion neurons are just beginning to respond to sound; later embryonic stages (E18–E19); and after hatching (P0–P2). We used in vitro whole cell patch electrophysiology to explore physiological changes in SON. Age-related changes were observed at the level of a single spike and in multispiking behavior. In particular, tonic behavior, measured as a neuron's ability to sustain tonic firing over a range of current steps, became more common later in development. Voltage-clamp recordings and biophysical models were employed to examine how age-related increases in ion currents enhance excitability in SON. Our findings suggest that concurrent increases in sodium and potassium currents underlie the emergence of tonic behavior.

NEW & NOTEWORTHY This article is the first to examine heterogeneity of neuronal physiology in the inhibitory nucleus of the avian auditory system and demonstrate that tonic firing here emerges over development. By pairing computer simulations with physiological data, we show that increases in both sodium and potassium channels over development are necessary for the emergence of tonic firing.

chick brain stem; excitability; GABA; ionic currents; superior olive

INTRODUCTION

Inhibitory feedback is widespread in the nervous system and crucial for neural functions including sensory processing. Within sensory systems, inhibition is often driven by, and thus scaled to, stimulus-driven excitation (Anwar et al. 2017). The resulting inhibitory feedback has a posited function toward gain control, which enhances various aspects of sensory processing. In the auditory system, for instance, gain control is important for preserving neural calculations of sound features in noisy environments (Willmore et al. 2014). The disruption of gain control following hearing loss has been implicated in auditory disorders such as tinnitus and hyperacusis (Auerbach et al. 2014; Richardson et al. 2012). Thus a balance between levels of excitation and inhibitory feedback must be tightly regulated in the healthy auditory system.

A useful system for examining this regulation is the avian auditory brain stem, which hosts sensory processing circuitry with connectivity suggestive of a gain control function for the main source of inhibition, the superior olivary nucleus (SON) (Burger et al. 2005). In this system, shown in Fig. 1, auditory nerve activity drives two primary auditory nuclei, nucleus angularis (NA) and nucleus magnocellularis (NM). While NA has been proposed to code for diverse aspects of a sound stimulus, including sound level (MacLeod and Carr 2007), NM plays a clear role in the coding of sound timing, containing neurons that phase-lock with sound stimuli (Sullivan and Konishi 1984; Takahashi et al. 1984). Through bilateral input from NM, a second-order nucleus, nucleus laminaris (NL), compares arrival time at the two ears. NA and NL drive activity in SON, which contains both level- and timing-sensitive neurons (Coleman et al. 2011). SON, in turn, provides a general inhibitory feedback through GABAergic projections that branch to provide shared input to NA, NM, and NL (Burger et al. 2005). This inhibitory feedback improves the encoding by NM and NL of sound timing information, particularly at high sound levels (Fukui et al. 2010; Nishino et al. 2008).

Either too little or too much inhibition can be detrimental to this brain stem circuit. Lesions of SON, or local GABA blockade, reduce specificity of timing coding in NM and NL (Fukui et al. 2010; Nishino et al. 2008). In contrast, excess inhibition in the absence of excitatory drive can damage the timing circuit, causing changes in ribosomes of NM neurons that are associated with neuronal death (Carroll and Hyson 2016). Thus physiological and metabolic data indicate that proper levels of SON activity must be maintained for proper circuit function.

Inhibitory feedback circuits in the brain must regulate the degree of descending inhibition based on the amount of ascending excitatory drive. This is unlikely to be a simple

Address for reprint requests and other correspondence: R. L. Hyson, Dept. of Psychology, Florida State Univ., 1107 W. Call St., Tallahassee, FL 32306-4301 (e-mail: hyson@psy.fsu.edu).

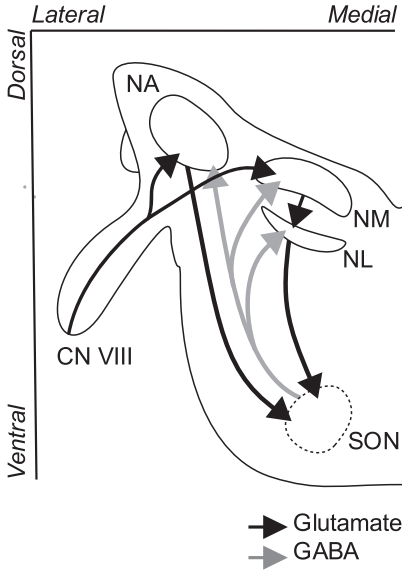

Fig. 1. Schematic of chick auditory brain stem. Input to the auditory nerve (CN VIII) provides glutamatergic drive to the primary auditory nuclei, nucleus angularis (NA) and nucleus magnocellularis (NM). NM, in turn, provides glutamatergic input to nucleus laminaris (NL). Together, NA and NL provide glutamatergic input to the superior olivary nucleus (SON). In turn, SON provides shared inhibitory feedback to NA, NM, and NL through branching GABAergic projections.

one-to-one relationship since neurons integrate synaptic drive and shape the corresponding output. The input-output function of neurons depends not only on the strength and pattern of synaptic inputs but also on the intrinsic properties of those neurons. Intrinsic properties are shaped by ion channel expression and thus are potentially malleable. Changes in intrinsic properties have been implicated in sensory plasticity (Mozzachiodi and Byrne 2010) and in multisensory functions like memory formation (Oh and Disterhoft 2015). In the auditory brain stem, intrinsic changes—for example, in the expression of voltage-gated Na^+ and K^+ channels—could influence the response of SON neurons to excitatory drive by altering the probability or frequency of firing action potentials and thus the pattern of GABA release in NA, NM, and NL.

During development, a challenge for the auditory system is how to adjust inhibitory feedback as the ear and ascending auditory pathway become more active. As noted, improper tuning of the input-output function of SON could lead to toxicity or disruption of auditory processing. We used SON to examine whether intrinsic electrical properties change during a vulnerable developmental time period, when ascending input to the SON begins to emerge, and when the bird begins to be exposed to airborne sounds. In light of the proposed role of SON in gain control, we hypothesized that increased brain stem excitation during this period would be paralleled by increased excitability of SON neurons.

Using in vitro whole cell patch clamp, we examined the intrinsic input-output relationships of SON neurons at three developmental time points: early in auditory development, embryonic days 14–16 (E14–E16), a time point at which cochlear ganglion neurons are just beginning to respond to sound but are still maturing in physiological phenotype (Galicia et al. 2015; Jones et al. 2006); later stages of embryonic development (E18–E19); and after hatching (P0–P1). This range includes a developmental period (E13–E17) during which GABAergic terminals in NM and NL dramatically increase, suggesting matured hardwiring of the inhibitory projections of SON (Korn et al. 2012). Using current clamp, we observed a developmental increase in neuronal excitability, particularly tonic behavior, supporting our hypothesis. To understand the mechanism for the increased excitability, we used the voltage-clamp technique to identify changes in Na^+ and K^+ conductances. Use of a computational biophysical model helped to integrate the current- and voltage-clamp data, providing additional insight into how the developmental changes in Na^+ and K^+ channel expression might bring about the developmental changes in electrophysiological responses that we observed. In particular, developmental increases in these channel types support the progression from a cell that spikes only once when depolarized to a cell that spikes tonically upon depolarization.

METHODS

Subjects. Twenty-four chicks (*Gallus gallus domesticus*) between the ages of P0 and P2 and 44 embryos between ages E14 and E19 were used in these experiments. Eggs were obtained from Charles River (North Franklin, CT) and incubated and hatched at Florida State University facilities. All experimental procedures were reviewed and approved by the Florida State University Animal Care and Use Committee.

Slice preparation. Subjects were deeply anesthetized on ice, if younger than E20, or with isoflurane, if older than E20. After decapitation, the skull was blocked coronally between the caudal forebrain and mesencephalon and submerged in artificial cerebrospinal fluid (aCSF) perfused with 95% O_2-5% CO_2. aCSF consisted of double-deionized water containing (in mM) 130 NaCl, 26 $NaHCO_3$, 3 KCl, 2 $MgCl_2 \cdot 5H_2O$, 2 $CaCl_2 \cdot 2H_2O$, 1.23 $NaH_2PO_4 \cdot H_2O$, and 10 dextrose and was warmed to ~35°C for the duration of the slice preparation.

The skull, forebrain, and cerebellum were removed from the blocked section, and the remaining brain stem was mounted with superglue on the stage of a vibrating blade microtome and resubmerged in warm oxygenated aCSF. Two hundred- to three hundred-micrometer coronal sections were collected. Sections were transferred to a separate chamber of warm oxygenated aCSF in which they were incubated for at least 30 min, gradually cooling to room temperature.

Recording conditions for electrophysiology. After incubation, a section was transferred to a chamber and superfused with room temperature (~23°C) oxygenated aCSF for the duration of the experiment. With the use of a light microscope, SON was identified with a stereotaxic atlas (Puelles et al. 2007) by its ovoid morphology and ventrolateral location relative to other structures, including NL and cranial nerves VII and VIII.

Glass capillary electrodes with resistances between 1.5 and 12 MΩ were filled with intracellular solution containing (in mM) 100 K-gluconate, 5 $MgCl_2$, 10 EGTA, 2 Mg-ATP, 0.3 Na_3-GTP, and 40 HEPES, pH adjusted to 7.2–7.3 with KOH. For experiments measuring sodium conductance (g_{Na}), an alternate cesium-based intracellular solution was used to block potassium channels, containing (in mM) 150 CsCl, 10 NaCl, 0.2 EGTA, and 10 HEPES, pH adjusted to 7.3–7.4 with CsOH. A filled electrode was lowered into SON and manipulated to approach the surface of a single neuron. When contact with the membrane was indicated by increased electrode resistance, negative pressure was applied to attain a whole cell patch. Measurements used an Axoclamp 700B amplifier with the feedback resistor set to 50 MΩ. The junction potential between the external and internal solutions was 5 mV and is uncorrected in the data presented.

The membrane potential of the patched cell was monitored, and cells that were spontaneously active or maintained a resting mem-

brane potential depolarized beyond −40 mV were excluded from analysis. Membrane capacitance (C_m), membrane resistance (R_m), and time constant were recorded with the Axoclamp membrane test. For voltage-clamp recordings, with Multiclamp Commander (Axon Instruments) C_m and electrode resistance parameters were adjusted in whole cell mode to reduce the transient artifact, and series resistance was compensated for by at least 80%.

Current-clamp experiments. In current-clamp mode, depolarizing currents were applied for 300 ms, typically beginning with 0 pA and increasing in increments of 10 pA up to 250 pA. Above 250 pA, currents were increased in 50-pA increments up to 1,250 pA. The voltage responses were recorded at a 20-kHz sampling rate, filtered at 1 kHz, and stored for subsequent off-line analysis.

Based on neuronal response to these protocols, a neuron's voltage behavior was characterized with custom analysis software using MATLAB (MathWorks). This software first applied a Savitzky-Golay filter to the voltage trace. To identify the rapid rise that initiates an action potential, the filtered trace was scanned for time points at which the derivative of the voltage exceeded 300 mV/ms. For each such time point the subsequent local maximum and minimum were located, and from these the amplitude was calculated. This amplitude was compared to a minimal amplitude, which was set to 5 mV for the first spike upon depolarization and was set for subsequent spikes to half of the previous spike's amplitude. These distinguishing features differentiated between spikes and subthreshold oscillations and allowed the quantification of the number of spikes (N_{spikes}) elicited at each current. For each neuron, the lowest applied current for which $N_{spikes} \geq 1$ defined the rheobase. For each current, if at least one spike was generated, features of the first spike were analyzed, including its width (time between action potential rise time and minimum voltage during afterhyperpolarization), rise time, fall time, rise and fall rate, maximal voltage, minimum voltage during afterhyperpolarization, amplitude, and delay before spiking.

If the applied current generated more than one spike, the interspike interval (ISI) was defined as the time between the last two spikes. This was compared to the average time between spikes at that applied current for the neuron (300 ms/N_{spikes}). If the former divided by the latter was between 0.85 and 1.15, the neuron was considered tonic for the applied current. At currents that did not elicit tonic behavior, steady-state membrane voltage was measured.

Voltage-clamp experiments. After current-clamp experiments, leak and potassium currents were examined in a subset of neurons with voltage-clamp and pharmacological manipulations. Each neuron was held at −90 mV, a potential at which most voltage-gated channels are deactivated. Subsequently, the cell was stepped to membrane potentials ranging from −110 to 10 mV, in 10-mV increments. Bath-applied tetrodotoxin (TTX), diluted to 1 μM, was used to block voltage-gated Na^+ currents. Neurons in which TTX reduced inward currents by <50% were excluded. In the remaining neurons, TTX blocked an average of 88% of the inward currents, and the extent of blockade was similar between age groups.

The remaining steady-state current, I_{Tot}, was assessed by averaging the current over a 25-ms period near the end of each voltage step. To measure leak current, a trend line was fit to the steady-state currents at membrane potentials of −110, −100, −90, and −80 mV, a voltage range over which K^+ channels are inactive. We did not consider in our analyses other currents that might be activated by hyperpolarization, such as currents through the hyperpolarization-activated cation channel (I_h), which may contribute to the measured leak. The slope of the trend line defined leak conductance (g_L), and the *x*-intercept defined leak reversal potential (V_L). This trend line was also used to calculate leak current at higher potentials. At potentials at and above −90 mV, calculated leak current was subtracted from I_{Tot} to assess the portion of current mediated by potassium, I_K. In some neurons, I_K was further dissected by bath application of 100 μM fluoxetine (FLX), which blocks $K_v3.1$-containing high-threshold K^+ channels (Sung et al. 2008). After FLX application, steady-state current was adjusted for I_L and subtracted from I_K to measure the high-threshold K^+ current (I_{HT}). Compared with I_{HT}, the remaining I_K not blocked by FLX was activated at lower voltages and was used as a measurement of the low-threshold K^+ current (I_{LT}). Maximal conductances g_{HT} and g_{LT} were measured as the change in conductance from a holding level of −90 mV to a steady-state conductance measured at a step to 10 mV.

To measure Na^+ currents, a cesium-based intracellular solution was used to block K^+ currents, which depolarized neurons. As alternative confirmation of cell health, Na^+ currents were only measured for stable neurons with access resistance < 15 MΩ. In a subset of experiments, extracellular solution also contained 2 mM TEA-Cl and 0.2 mM 4-AP. After an initial holding potential of −90 mV, neurons were stepped to potentials ranging from −110 to 10 mV, and current responses were recorded at a high sampling rate of 500 kHz. To ensure isolation of I_{Na}, in each neuron the experiment was repeated after bath application of TTX. The amplitude of the TTX-sensitive transient was measured from the subtraction of pre- and post-TTX recordings. The maximal deviation during a steady-state current at −90 mV was considered to be noise, and this value was subtracted from the step-induced measured currents. This was done to avoid overestimating Na^+ currents. Maximal sodium conductance g_{Na} was calculated for each neuron, as by Hong et al. (2016), at the potential *V* that maximized the average amplitude of the Na^+ current across neurons of the same age group, accounting for the driving force on this potential under experimental conditions using V_{Na} = 69.56 mV based on sodium concentrations in the aCSF and Cs-based intracellular solution: $g_{Na} = I_{Na}/(V - V_{Na})$.

Statistical analysis. All statistical analyses were performed in SPSS. For single measures (resting membrane potential, rheobase, C_m, V_L, g_L, g_{LT}, g_{HT}, g_{Na}) means were compared to test statistical differences between age groups. N_{spikes} was recorded for a range of currents common to all neurons, and responses to individual current steps in this range were treated as repeated measures in fitting each neuron to a general linear model. Similarly, repeated measures I_K, I_{LT}, I_{HT}, and I_{Na} over a range of voltage steps were analyzed by analysis of variance (ANOVA).

For other current-clamp measures, the range of currents that could be analyzed varied based on each neuron's unique firing behavior. In particular, ISI could only be measured at currents that elicited tonic behavior, while steady-state voltage could only be measured at currents that did not elicit tonic behavior. Other measurements of spike features—delay, amplitude, maximum voltage during action potential, minimum voltage during afterhyperpolarization, width, rise time, rise rate, fall time, and fall rate—could not be taken at subthreshold currents, which varied between neurons. Because of these missing data, a simple factorial ANOVA could not be performed. Instead, age-related differences over a range of applied currents were analyzed by fitting mixed-effects models to the sample of observed values for each measure. This analysis treats the spike feature in response to each applied current as a within-neuron repeated measure to determine how change in that feature across repeated measures varies with age, allowing the inclusion of neurons regardless of the range of applied currents for which data were available.

To optimize the fit of mixed-effects models, the data for a given spike feature were initially examined across age groups. Neurons within this sample population were first fit to a quadratic equation ($Y = aI^2 + bI + c$; where *Y* is the parameter of interest and *I* is the applied current), allowing random variation of intercept (*c*), slope (*b*), and the quadratic factor (*a*). As shown in Table 1, spike amplitude, maximum voltage during action potential, spike width, spike rate, fall rate, fall time, steady-state voltage, and ISI were best fit by this type of equation. If this fit did not demonstrate a statistically significant ($P < 0.05$) random effect of this quadratic factor, a second fit was tested that held this factor constant across neurons, only allowing random variation of intercept and slope. Minimum voltage during afterhyperpolarization, delay to spike, rise rate, and rise time fit this type of equation. If this second fit did not demonstrate a reliable

Table 1. *Mixed-effect models: current-clamp features across age groups*

	Fixed Variables			Random Variables		
	Intercept	Slope	Quad	Intercept	Slope	Quad
Delay, ms	31.42	−7.20	0.038*	1,070.89	310.33	
Sp1amp, mV	54.82	−0.95*	0.025*	393.71	1.63	0.002
Sp1min, mV	−44.82*	1.82	−0.026	90.41	1.02	
Sp1max, mV	10.17	0.83	−0.003***	273.64	3.17	0.001
Sp1width, ms	12.09*	−0.53	0.012	41.39	0.34	0.0003
Rise rate, mV/ms	27.59*	−1.38	0.060	555.78	2.18	
Fall rate, mV/ms	13.10*	0.40*	−0.008*	158.80	0.56	0.0004
Sp1 rate, mV/ms	15.05*	0.02	0.010	228.93	1.24	0.001
Rise time, ms	5.55*	−0.23*	0.004	11.96	0.01	
Fall time, ms	6.32*	−0.29	0.008	9.69	0.06	0.0001
Steady state, mV	−36.53	4.72*	−0.082***	72.80	18.08	0.003
ISI, ms	37.11	11.39	−0.113	6,393.48	258.26	0.299

This analysis uses different current injections as a within-subject variable to determine whether there are age-dependent differences in the current-response growth functions for the various measures. Fixed variables represent the mean values used to fit the given feature's growth curve across the whole population of cells. Random variables represent the degree to which the model allows individual neurons to vary from those mean values. An in-depth description of these growth curves can be found in METHODS. These models were created for experimental measures that could not be treated as repeated measures: delay to spike (delay), amplitude (amp) of first spike (Sp1), minimum voltage during first spike afterhyperpolarization (min), maximum voltage during first spike (max), width of first spike (width), rate of rising phase during first spike (rise rate), rate of falling phase during first spike (fall rate), overall rate of first spike (rate), length of falling phase during first spike (fall time), steady-state voltage (steady state), and interspike interval (ISI). Statistical analyses test whether a fixed variable significantly differs between age groups: $*P < 0.05$, $***P < 0.01$. Statistical differences in intercept indicate an overall effect of Age, while differences in slope or the quadratic factor indicate an Age × Current interaction.

random effect of slope, a third fit was tested, in which neurons were fit to a linear equation ($Y = bI + c$), allowing random variation of intercept and slope. If there was no reliable random effect of slope, a final fit was tested, fitting neurons to a linear equation only allowing random variation of intercept between neurons.

Once the equation type best fitting a given spike feature was identified, growth curves of different age groups were compared to identify any age-related changes in spiking behavior. There were no trends toward age-related changes in ISI, so this feature was not further explored. All other measured parameters showed a statistically significant difference between age groups in intercept, slope, or quadratic factor. A difference in intercept indicates an overall effect of Age, whereas differences in slope or quadratic factors indicate an Age × Current interaction. Whether this interaction is observed in the linear or quadratic factor is indicated in Table 1 and Table 2.

Model neurons. Single-compartment biophysical models were created based on those employed by Daou et al. (2013), representing SON neurons at early embryo, late embryo, and hatchling time points. Each biophysical model contained four currents: I_L, I_{Na}, I_{HT}, and I_{LT}. Equations representing I_L, I_{Na}, and I_{HT} were based on those previously published by Daou et al. (2013), while those representing I_{LT} were based on those previously published by Rothman and Manis (2003). Aspects of these equations, particularly membrane time constants, were adjusted slightly to better reflect the action potential properties of SON neurons than neurons of the zebra finch HVC and mammalian cochlear nucleus on which these original models are based. Maximal conductance values for each current, g_L, g_{Na}, g_{HT}, g_{LT}, V_L, and cell capacitance (C_m) were averaged for each age group in our electrophysiological experiments. Other reversal potentials, V_{Na} and the K^+ reversal potential (V_K), were calculated based on known concentrations in the aCSF and intracellular solution. Equations for the ionic currents are

$$I_L = g_L(V - V_L) \quad (1)$$

$$I_{Na} = g_{Na} m_\infty^3(V) h(V - V_{Na}) \quad (2)$$

$$I_{HT} = g_{HT} n^4(V - V_K) \quad (3)$$

$$I_{LT} = g_{LT} y^4 z(V - V_K) \quad (4)$$

where $m_\infty(V)$ is the instantaneous activation of Na^+ channels, n and y are activation variables, and h and z are inactivation variables. The membrane potential (V) of the model neuron with these currents satisfies

$$\frac{dV}{dt} = (I_{ap} - I_L - I_{Na} - I_{HT} - I_{LT})/C_m \quad (5)$$

The activation and inactivation variables change over time according to

$$\frac{dx}{dt} = \frac{x_\infty(V) - x}{\tau_x} \quad (6)$$

where $x = h, n, y, z$. The equilibrium functions are

Table 2. *Mixed-effect models: current-clamp features by age group*

	Early Embryo			Late Embryo			Hatchling		
	Intercept	Slope	Quad	Intercept	Slope	Quad	Intercept	Slope	Quad
Delay, ms	43.74	−12.70	0.032	29.58	−5.95	0.046	21.93	−3.60	0.029
Sp1amp, mV	47.97	−2.30	0.071	57.98	−0.96	0.031	59.04	−0.08	0.002
Sp1 min, mV	−37.82	2.17	−0.035	−46.97	1.41	−0.024	−48.47	1.56	−0.021
Sp1max, mV	10.62	−0.01	0.021	9.889	0.90	−0.005	10.80	1.30	−0.017
Sp1width, ms	17.17	−0.77	0.018	11.34	−0.49	0.011	8.14	−0.30	0.006
Rise rate, mV/ms	11.23	−0.38	−0.001	32.61	−1.91	0.068	33.55	−1.31	0.053
Fall rate, mV/ms	7.94	−0.37	0.030	11.22	0.46	−0.009	21.01	0.86	−0.019
Sp1 rate, mV/ms	7.66	−0.21	0.009	14.04	0.08	0.008	23.73	0.002	0.019
Rise time, ms	8.52	−0.43	0.009	4.74	−0.18	0.003	4.10	−0.17	0.003
Fall time, ms	8.24	−0.29	0.009	6.47	−0.34	0.009	4.09	−0.19	0.005
Steady state, mV	−33.90	6.73	−0.107	−38.84	3.90	−0.075	−36.74	2.95	−0.056

Fixed variables by age group represent the mean factors used to fit a given feature's growth curve across the subset of cells in each age group. These models were created for experimental measures that could not be treated as repeated measures: delay to spike (delay), amplitude (amp) of first spike (Sp1), minimum voltage during first spike afterhyperpolarization (min), maximum voltage during first spike (max), width of first spike (width), rate of rising phase during first spike (rise rate), rate of falling phase during first spike (fall rate), overall rate of first spike (rate), length of falling phase during first spike (fall time), steady-state voltage (steady state) and interspike interval (ISI).

Table 3. *Parameters for model neurons*

	Early Embryo	Late Embryo	Hatchling
Measured parameters			
C_m, pF	58.2 ± 2.1 (n = 31)	42 ± 1.5 (n = 29)	36 ± 7.2 (n = 20)
V_L, mV	−46.3 ± 5.5 (n = 12)	−40.6 ± 2.6 (n = 16)	−26.3 ± 10.4 (n = 13)
g_L, nS	7.3 ± 1.3 (n = 12)	4.6 ± 0.2 (n = 16)	12.7 ± 5.5 (n = 13)
g_{HT}, nS	0.2 ± 0.4 (n = 8)	2.8 ± 0.5 (n = 8)	5.5 ± 1.3 (n = 10)
g_{LT}, nS	3.7 ± 1.1 (n = 8)	6.8 ± 0.4 (n = 8)	16.2 ± 4.9 (n = 10)
g_{Na}, nS	33.8 ± 4.9 (n = 10)	53.6 ± 12.2 (n = 9)	79.2 ± 17.4 (n = 6)
Parameters based on solution			
V_{Na}, mV	158.1		
V_K, mV	−97		
Other constants			
τ_h, ms	5		

Parameters measured in each age group are shown as averages ± SE.

$$h_\infty(V) = \frac{1}{1 + \exp\left(\frac{V + 50}{7}\right)} \quad (7)$$

$$m_\infty(V) = \frac{1}{1 + \exp\left(\frac{V + 35}{-5}\right)} \quad (8)$$

$$n_\infty(V) = \frac{1}{1 + \exp\left(\frac{V + 30}{-5}\right)} \quad (9)$$

$$y_\infty(V) = \left\{\frac{1}{1 + \exp\left[-\frac{(V + 48)}{6}\right]}\right\}^{-0.25} \quad (10)$$

$$z_\infty(V) = 0.5\left[\frac{1}{1 + \exp\left(\frac{V + 71}{10}\right)}\right] + 0.5 \quad (11)$$

The time constant equations are

$$\tau_n(V) = 5\left[\frac{10}{\cosh\left(\frac{V + 30}{-10}\right)}\right] \quad (12)$$

$$\tau_y(V) = \frac{100}{6\exp\left(\frac{V + 60}{6}\right) + 16\exp\left(-\frac{V + 60}{45}\right)} + 1.5 \quad (13)$$

$$\tau_z(V) = \frac{1{,}000}{\exp\left(\frac{V + 60}{20}\right) + \exp\left(-\frac{V + 60}{8}\right)} + 50 \quad (14)$$

All values of parameters used in biophysical models, including the voltage-independent time constant, τ_h, are listed in Table 3.

RESULTS

SON neurons become more excitable during development. In current-clamp experiments using hatchling tissue, SON neurons varied in their response to a prolonged (300 ms) depolarizing current. The smallest amount of current capable of eliciting an action potential, rheobase, varied between neurons, 49 pA ± 9 pA (n = 25). As applied currents increased beyond rheobase, some, but not all, SON neurons displayed sustained tonic firing throughout the current step. Figure 2*A* shows example responses of three hatchling SON neurons to a subset of applied currents. Some neurons did not exhibit tonic behavior at any applied current (Fig. 2*Ai*), while others spiked repetitively to some range of currents. The between-neuron variations in this range are shown in Fig. 2*B*, in which letters on the right denote neurons recorded from the same bird and arrowheads denote the three neurons with responses shown in Fig. 2*A*. Many neurons spiked tonically over a wide range, such as *neuron iii*, which spiked tonically at any applied current between 20 and 400 pA. Others exhibited tonic activity only in response to a narrow range of applied currents, such as *neuron ii*, which only spiked tonically at 80 and 100 pA. For some neurons, the range of tonic behavior was not continuous. This surprising intermittent tonic behavior might be due to factors not accounted for in our experiments, including spontaneous excitatory postsynaptic potentials. No matter the range,

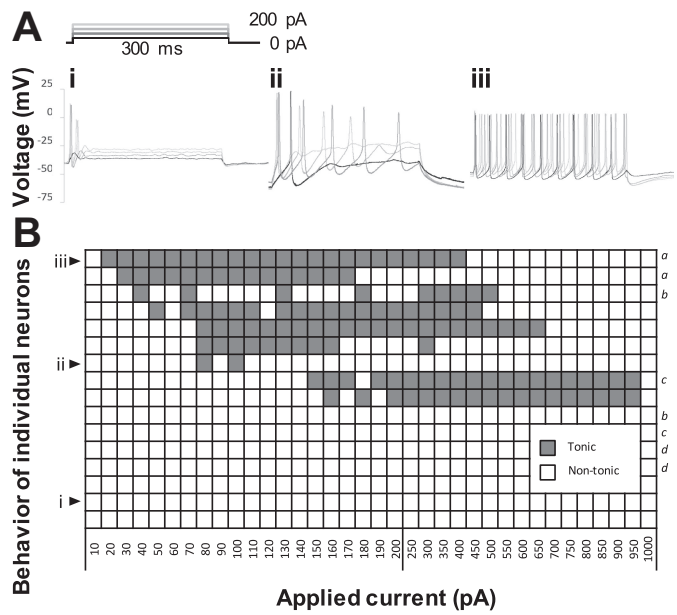

Fig. 2. Heterogeneity within the hatchling SON. *A*: voltage behaviors in response to prolonged application of depolarizing currents (*inset:* 50, 100, 150, 200 pA) of 3 different neurons (*i–iii*) from hatchling SON. *B*: voltage behaviors vary between neurons, with many (9 of 16) displaying tonic behavior at a subset of applied currents. In 4 subjects, multiple SON neurons were recorded; the rows representing these neurons are marked on *right* for *subjects a*, *b*, *c*, and *d*. Arrowheads designate the cells displayed in *A*.

however, neurons that exhibited tonic behavior in response to at least one applied current constituted 56% of SON neurons (9/16) in the hatchling.

In contrast, SON neurons at earlier time points required larger applied currents to fire and displayed less excitability. Average rheobase was 76 ± 2 pA in the late embryo and 129 ± 5 pA (n = 24) in the early embryo. A comparison of means showed a statistically significant effect of Age [$F(2,84) = 5.63$; $P = 0.005$], and a post hoc (Student-Newman-Keuls) test showed that the early embryo neurons displayed a significantly higher rheobase than late embryos or hatchlings.

Neurons at earlier time points were less likely to exhibit tonic behavior (Fig. 3*A*). In late embryos 26% (9/35) of neurons exhibited tonic behavior, and in early embryos only 12% of neurons did (3/26). These changes in spiking behavior were reflected in the average number of spikes (N_{spikes}) fired throughout a range of 300-ms applied currents, shown in Fig. 3*B*. Over a range of applied currents, there was a developmental increase in N_{spikes}. An ANOVA revealed that an Age × Current interaction [$F(50,1275) = 5.70$; $P < 0.001$] and a between-subject effect of Age [$F(2,51) = 14.69$; $P < 0.001$] were statistically significant, and a post hoc analysis (Student-Newman-Keuls) showed differences between the early embryo and hatchling. Most markedly, around 250 pA, early embryos fired 1.12 ± 0.39 spikes (n = 17), late embryos 2.72 ± 0.82 spikes (n = 21), and hatchlings 10.29 ± 2.3 spikes (n = 16). When larger currents were applied, spikes began to adapt in amplitude over the course of the tonic train because of depolarization block (Fig. 3*B*, *inset*). This amplitude adaptation was graded, creating a blurred distinction between the initial spikes and subsequent smaller oscillations. Therefore, to objectively count N_{spikes}, oscillations with slower rise times and amplitudes less than half that of the previous spike were not counted as spikes (see METHODS). At higher applied currents, tonic spiking was replaced by a depolarized steady-state voltage, causing a decrease in the number of spikes produced. Because of this decrease, there are no apparent differences in N_{spikes} between the age groups at applied currents above 1,050 pA.

In addition to changes in spiking behavior, age-related changes also occurred at the level of a single action potential. Values used to fit mixed-effects models of each feature to the entire sample population and to each age group are provided in Table 1 and Table 2. Many of the observed changes are evident in the sample responses of SON neurons from an early embryo

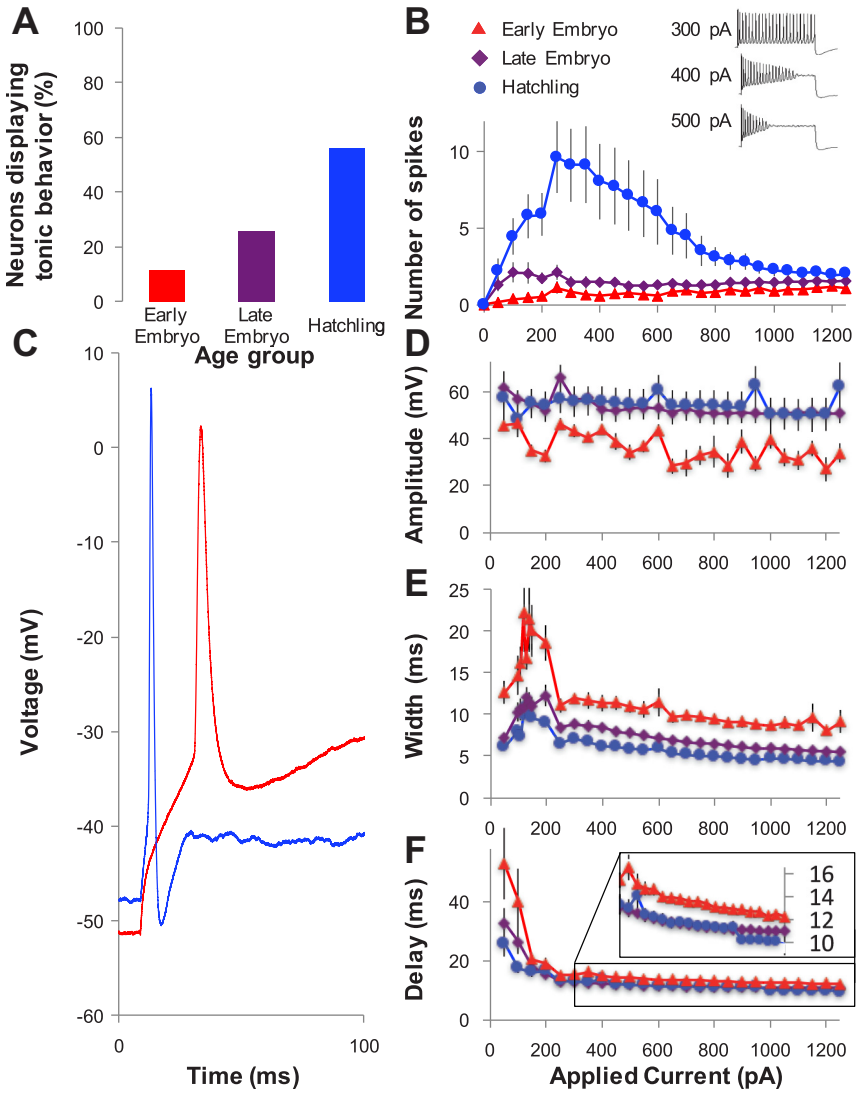

Fig. 3. Age-related increase in excitability of SON neurons. *A*: % of neurons exhibiting tonic behavior in response to at least 1 applied current increases with age. *B*: mean number of action potentials fired in response to various applied currents increases with age. At higher applied currents, depolarization block occurs, eliminating tonic behavior (*inset*: example from hatchling). *C*: action potentials in SON in the early embryo (red) vs. in the hatchling (blue) in response to a 100-pA applied current. This example demonstrates the developmental increase in amplitude and decreases in width and delay to spike, shown over a wider range of applied currents in *D*–*F*.

and a hatchling to a 100-pA depolarizing current, shown in Fig. 3*C*. Across development, action potentials became larger in amplitude, as shown in Fig. 3*D* (mixed-effect model; Age × Current interaction, $P = 0.001$). Underlying the change in amplitude were an age-related increase in maximal voltage during the action potential peak (mixed-effect model; Age × Current interaction, $P = 0.019$) and an age-related decrease in the minimal voltage during the afterhyperpolarization (mixed-effect model; Age, $P = 0.002$). These maxima and minima, across a range of applied currents, are depicted as average values for each age group in Fig. 4, *bottom*, along with the statistical models fit to them in Fig. 4, *top*. Enhanced variability of these depicted measures in the early embryo appears due in part to more variable steady-state voltage in this age group. Supporting this hypothesis, variability in spike amplitude (not shown), which considers maximum and minimum voltage independent of steady-state voltage, was comparable between age groups.

Action potentials also changed in timing. Early in development, spikes occurred more slowly, spike width decreasing with age (mixed-effect model; Age, $P < 0.001$), as shown in Fig. 3*E*, even when normalized to spike amplitude (mixed-effect model; Age, $P = 0.001$). The change in spike width was a result of changes in both rising and falling phases. Rise time decreased with age (mixed-effect model; Age, $P < 0.001$; Age × Current interaction, $P = 0.01$), even when normalized to amplitude (mixed-effect model; Age, $P = 0.031$). Fall time decreased with age (mixed-effect model; Age, $P < 0.001$), even when normalized to amplitude (mixed-effect model; Age, $P = 0.001$; Age × Current interaction, $P < 0.001$). There was also a developmental decrease in delay to first spike (Fig. 3*F*; mixed-effect model; Age × Current interaction, $P < 0.001$).

A final developmental change was observed in steady-state voltage, the average voltage reached by a neuron during a prolonged current that does not elicit tonic behavior. Neurons at older ages were less depolarized by applied currents, resulting in more polarized steady states (mixed-effect model; Age × Current interaction, $P = 0.005$). This difference is evident in the baseline achieved by the neurons in Fig. 3*C*; after the action potential, the early embryo neuron remains more depolarized by the continued current application than the hatchling neuron. There was no statistically significant difference in resting membrane potential between age groups [$V_m = -47.6 \pm 1.2$ mV in early embryo, -50.4 ± 1.3 mV in late embryo, -50.1 ± 1.6 mV in hatchling; $F(2, 87) = 1.32$; $P = 0.270$].

Developmental changes in membrane currents. Subsequent experiments were performed to examine factors that might contribute to the developmental increase in excitability. Previous reports have linked developmental changes in input resistance that influence aspects of voltage behavior in neurons of NM, NL, and the mammalian medial superior olive (Hong et al. 2016; Kuba et al. 2002; Scott et al. 2005). In contrast, we found no change in the related measure, R_m [54.09 ± 2.00 MΩ in early embryo, 54.76 ± 1.81 MΩ in late embryo, 55.64 ± 17.87 MΩ in hatchling; $F(2, 77) = 0.004$; $P = 0.996$]. Because a change in input resistance does not seem to account for the observed developmental changes, we examined which other membrane properties might. Average values of each membrane property, along with variability, are listed in Table 3. We first compared across ages the passive membrane properties, C_m and the leak current (I_L). C_m did not show a statistically significant change over development [$C_m = 58.2 \pm 2.1$ pF in early embryo, 42 ± 1.5 pF in late embryo, 36 ± 7.2 pF in hatchling; $F(2, 77) = 1.36$; $P = 0.26$]. In voltage-clamp experiments, I_L was assessed by measuring sustained currents over a range of hyperpolarizing potentials in the presence of TTX. There were no statistically significant between-group differences in either g_L [7.25 ± 1.3 nS in early embryo, 4.6 ± 0.2 nS in late embryo, 12.7 ± 5.5 nS in hatchling; $F(2, 38) = 1.80$; $P = 0.179$] or V_L [-46.3 ± 5.5 mV in early embryo, -40.6 ± 2.6 mV in late embryo, -26.3 ± 10.4 mV in hatchling; $F(2, 38) = 1.11$; $P = 0.34$], so this current was treated as a source of variability and subtracted from each cell's steady-state current to more accurately measure voltage-gated K^+ currents.

Voltage-gated K^+ currents were measured over a range of potentials as the difference between a neuron's total steady-state current and its leak current. Voltage-gated K^+ currents increased with membrane potential and over development, as

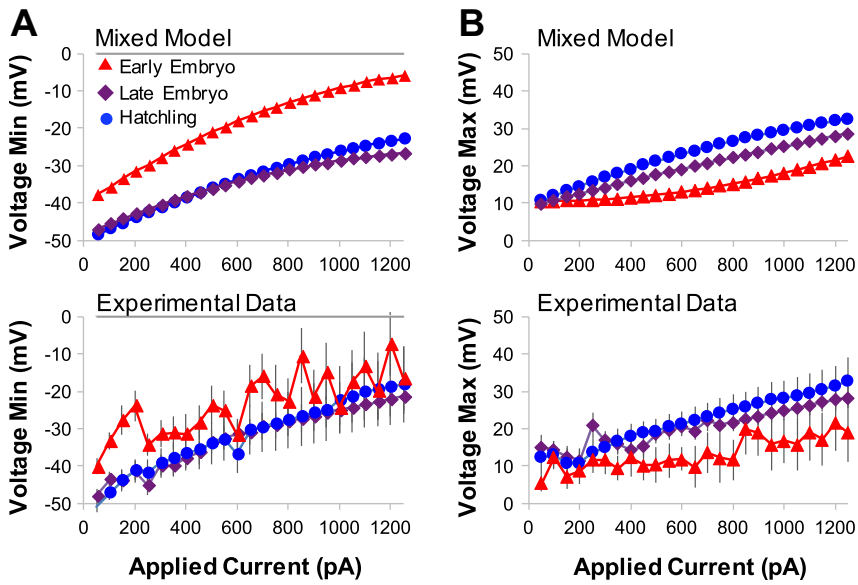

Fig. 4. Comparison of mixed-effect models and experimental data for spike features contributing to amplitude. *Bottom:* average experimental measurements of minimum voltage (*A*) and maximum voltage (*B*). *Top:* mixed-effect models fit to these data. Maximum voltage was best fit as a quadratic equation, allowing random variation of intercept, slope, and a quadratic factor. Minimum voltage was best fit as a quadratic equation, allowing random variation of intercept and slope. Intercept, slope, and quadratic factors for each model are shown as Sp1min and Sp1max in Table 2.

shown in Fig. 5*A*, *left*. An ANOVA yielded a statistically significant between-subjects effect of Age [$F(2, 38) = 6.48$; $P = 0.004$] and an Age × Voltage interaction [$F(20, 380) = 5.65$; $P < 0.001$]. In a subset of neurons, FLX was applied to further investigate components of the steady-state K^+ current. FLX is a potent blocker of the subunit $K_v3.1$ present in high-threshold K^+ channels and has previously been used in the chick nucleus magnocellularis to distinguish between high- and low-threshold K^+ currents (Hong et al. 2016). The effects of FLX differed between age groups, as shown in Fig. 5*A*, *center* and *right*. In SON, application of FLX had no apparent effect on K^+ currents in the early embryo but decreased steady-state currents at later ages. Figure 5*B* shows K^+ currents (I_{HT}) blocked by FLX. In an ANOVA, the between-subject effect of Age was not statistically significant [$F(2, 23) = 2.70$; $P = 0.088$]. However, Age × Voltage interaction was statistically significant [$F(20, 230) = 4.49$; $P < 0.001$], and comparison of means showed a statistically significant change in g_{HT} ($g_{HT} = 0.2 \pm 0.4$ nS in early embryo, 2.8 ± 1.3 nS in late embryo, 5.5 ± 1.3 nS in hatchling) [$F(2, 23) = 5.43$; $P = 0.012$]. Figure 5*C* shows the current that remained after FLX treatment. Like I_{HT}, this FLX-insensitive current increases with age. In an ANOVA, both between-subjects effects of Age [$F(2, 23) = 5.666$; $P = 0.010$] and the Age × Voltage interaction [$F(20, 230) = 3.56$; $P < 0.001$] were statistically significant, as was a comparison of means for g_{LT}: [$g_{LT} = 3.7 \pm 1.1$ nS in early embryo, 6.8 ± 0.4 nS in late embryo, 16.2 ± 4.9 nS in hatchling; $F(2, 23) = 3.91$; $P = 0.035$]. This current is present at hearing onset, is larger than I_{HT}, and—consistent with the low-threshold K^+ current—appears to activate at lower potentials than I_{HT}.

In a different set of neurons, voltage-clamp recordings were used to measure Na^+ currents, with K^+ currents blocked with a cesium-containing intracellular solution. I_{Na} was further isolated by recording a neuron's response to depolarization before and after the application of TTX. Figure 5*D* shows examples of these transient, inward currents. The currents are graded, emerging with sufficient depolarization and then decreasing in amplitude as the neuron is further depolarized toward the Na^+ reversal potential. I_{Na} amplitude was maximal at −20 mV in the early and late embryo and at −30 mV in the hatchling. Figure 5*E* shows an age-related increase in I_{Na} amplitude over a range of applied potentials. In an ANOVA, this increase was statistically significant as an Age × Voltage interaction [$F(44, 462) = 1.15$; $P = 0.022$], though not as a between-subject effect of Age [$F(2,21) = 1.82$; $P = 0.187$]. There was also a statistically significant age-related increase in g_{Na} [$g_{Na} = 33.8 \pm 4.9$ nS in early embryo, 53.6 ± 12.2 nS in

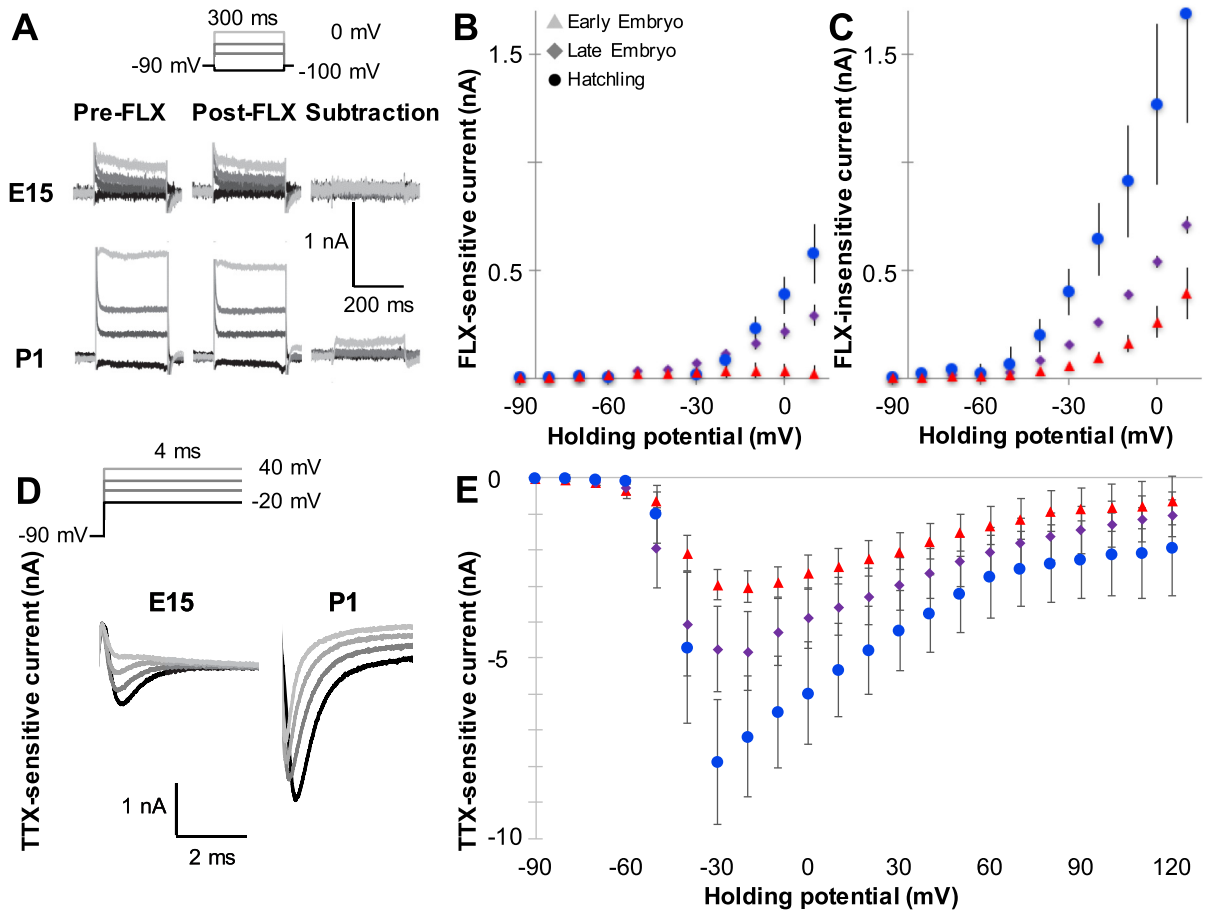

Fig. 5. Developmental changes in potassium and sodium currents. *A*: examples of outward currents following depolarization (*inset:* −60, −30, 0 mV) in an E15 and a P1 neuron before and after fluoxetine (FLX) treatment and the FLX-blocked component (subtraction of pre- and post-FLX recordings). These currents are larger in the P1 neuron and markedly reduced after FLX treatment. Inward currents at a step to −100 mV are shown to illustrate leak current. Capacitive transient currents have been clipped for clarity. *B*: outward currents blocked by FLX treatment increase across ages. *C*: outward currents unaffected by FLX treatment increase across ages. *D*: examples of transient inward currents blocked by TTX in E15 and P1 neurons in response to depolarization (*inset:* −40, −20, 0, 20, 40 mV). *E*: inward currents blocked by TTX increase across ages.

late embryo, 79.2 ± 17.4 nS in hatchling; $F(2,22) = 3.90$; $P = 0.036$].

Sodium currents are notoriously difficult to record with whole cell recordings in a slice preparation, where aspects of cell morphology, particularly axons and dendritic arborizations, interfere with flow of the holding current to produce space clamp issues (Armstrong and Gilly 1992; Bar-Yehuda and Korngreen 2008). These shortcomings in our voltage clamp are most evident in the hatchling, in which even the most depolarizing currents fail to inactivate I_{Na} (in Fig. 5*E*, see plateau at step potentials above 60 mV). Considering these technical issues, g_{Na} calculated for each age group serves only as an estimate, and future experiments could improve this estimate by reducing the extracellular Na^+ concentration, further lowering recording temperature, or measuring I_{Na} in an excised patch rather than the whole-cell patch performed here. Nonetheless, we are confident of the broader finding of a developmental increase in g_{Na} even though the magnitude of this change will lack precision. As shown in the following section, however, these estimates are sufficient to produce modeled current-clamp responses similar to those observed in experimental recordings. This correspondence gives additional confidence that the estimates obtained in the voltage-clamp recordings are not drastically inaccurate owing to poor quality voltage control.

Computational models connect developmental changes in conductances to voltage behavior. For each age group, a single-compartment biophysical model neuron was fit, using patch-clamp measurements of average capacitance, conductances (g_L, g_{HT}, g_{LT}, g_{Na}), and V_L, or those based on experimental conditions, V_{Na} and V_K. Because Na^+ and K^+ measurements required different intracellular solutions and drug applications, g_{Na} was measured in a different SON subsample than other parameters. Average measures for each age group, and degree of variation, are displayed in Table 3, along with parameters held constant between age groups. With these mean values, three resulting model neurons were built, representing average voltage behavior in the early embryo, late embryo, and hatchling. These biophysical models were used to test the hypothesis that observed changes in Na^+ and K^+ channels were sufficient to explain developmental changes in neuronal activity.

Current-clamp simulations using the resulting biophysical models are shown in Fig. 6*A* and Fig. 7*A*. Our varied parameters accounted for many of the changes in voltage behavior observed experimentally. Rheobase was one exception, as it was similar across age groups, suggesting that some developmental factors not included in the model decrease rheobase in vitro. Because 120 pA was rheobase in all three biophysical models, characteristics of the first spike were examined at this current step (Fig. 6*A*). Age-related changes similar to those observed in vitro were evident. Across ages, spike amplitude increased, through increased maximal voltage and a more severe afterhyperpolarization. Similarly, both rising and falling phases became more rapid, narrowing the spike width. Models of older cells also showed a reduction in delay to spike.

In the late embryo model, which displays a spike with a phenotype intermediate to early embryo and hatchling models, we varied g_{Na}, g_{HT}, and g_{LT} to examine how developmental changes in Na^+ and K^+ currents might contribute to parallel changes in spike features. The results for manipulation of g_{Na} are shown in Fig. 6*B*. A developmental increase in Na^+ current appears to drive the increase in spike amplitude. Lowering g_{Na} to the level of an early embryo eliminates the action potential, while increasing it to the level of a hatchling makes the spike larger. Increasing g_{Na} also has effects on kinetics, decreasing delay to spike and speeding up rise time. Effects of I_{HT} are more limited, primarily affecting the falling phase. With g_{HT} increased to the level of a hatchling neuron, the falling phase occurs more rapidly and reaches a more polarized minimum voltage during afterhyperpolarization, modestly increasing spike amplitude (Fig. 6*C*). Finally, decreasing g_{LT} to the level of an early embryo neuron increases the spike peak, while decreasing the delay to spike and rise time (Fig. 6*D*). Increasing g_{LT} has the opposite effect, and without a parallel increase in g_{Na} to a hatchling level, a hatchling level of g_{LT} eliminates the spike altogether. Thus the phenotype of the hatchling neuron, with a larger and narrower spike with less delay, is achieved through an increase in g_{Na} to increase spike amplitude and decrease the delay to spike and a parallel increase in g_{HT} to make the spike narrower. The developmental increase in g_{LT}

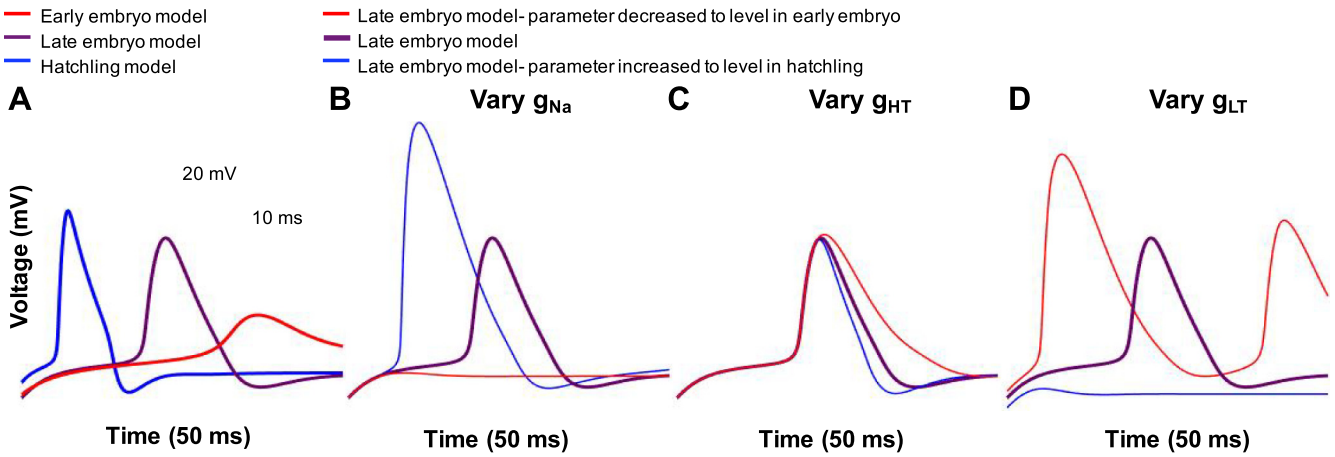

Fig. 6. Current contributions to features of a single spike. *A*: models exhibit age-related changes in voltage response to an applied current of 120 pA. Like the action potentials shown in Fig. 3*C*, spikes from these biophysical models increase in amplitude and kinetics at later developmental time points. *B–D*: the late embryo model was used in further simulations to examine how individual currents contribute spike features. In the late embryo model, other parameters are held constant during a 120-pA current step, while g_{Na} (*B*), g_{HT} (*C*), and g_{LT} (*D*) are decreased to the level of an early embryo or increased to the level of a hatchling.

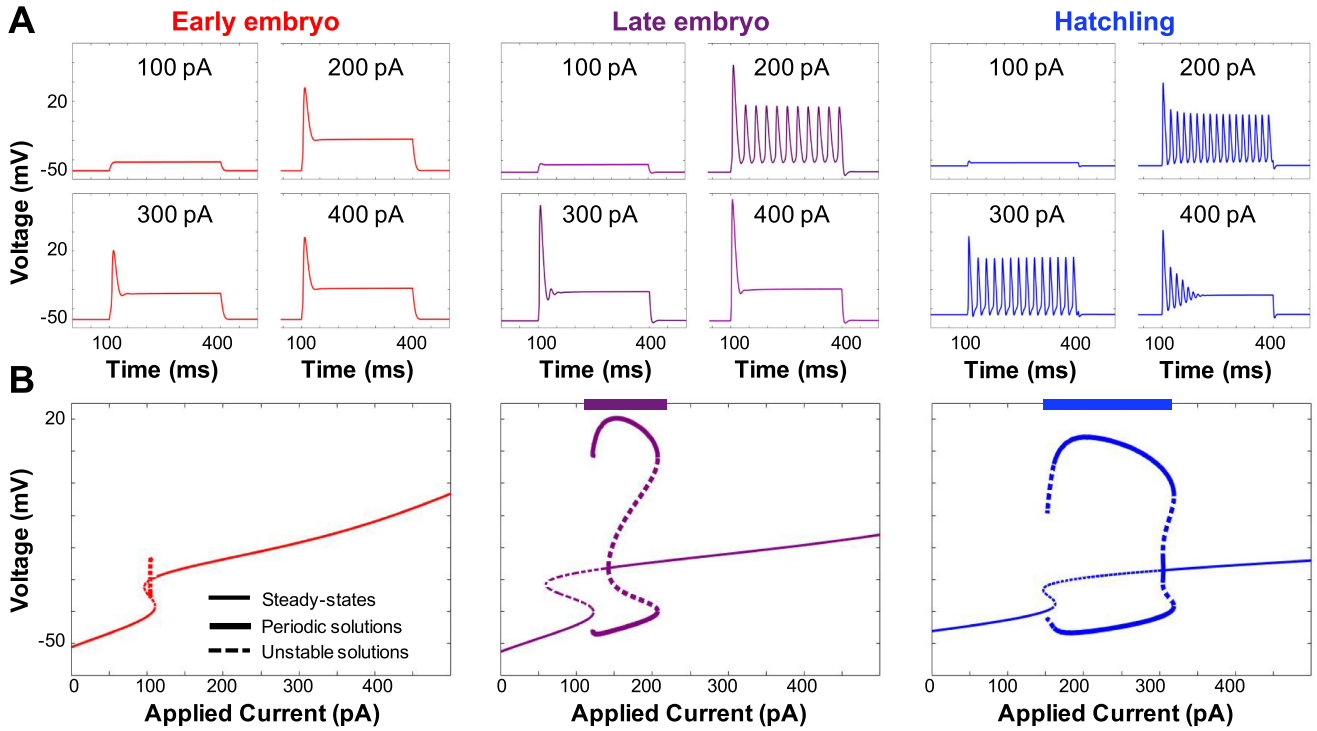

Fig. 7. Voltage behavior of model neurons. *A*: responses of model SON neurons based on early embryo, late embryo, and hatchling to a simulation similar to current-clamp experiments performed in vitro. *B*: bifurcation diagrams used to explore tonic behavior (stable periodic solutions) and steady-state voltage (stable steady states) over a range of applied currents. Note the increased range of the periodic branches, marked by a bar on the top axis, over development.

partially opposes the increased Na^+ conductance, and its impact on the single action potential is not evident.

Beyond the level of a single spike, models more broadly replicated developmental changes in voltage behavior observed in the in vitro recordings. Figure 7*A* shows that, while the early embryo model does not respond to any applied current with tonic behavior, models for older cells display a developmental increase in tonic firing and spike number, the same shift in voltage behavior observed in vitro.

To examine tonic behavior over a wider range of currents, bifurcation diagrams were created for each model neuron, as shown in Fig. 7*B*. These diagrams display the asymptotic, or long-term, membrane voltage in response to a range of applied currents, including steady-state and periodic solutions. Unstable solutions are included in Fig. 7*B* as a dashed line, but stable states (solid lines) hold more physiological relevance. The stable steady-state solutions in these diagrams are akin to the steady-state voltages measured in current-clamp experiments, as these solutions represent a neuron's response to prolonged current application with a fixed voltage, rather than with tonic spiking. Tonic spiking, in these bifurcation diagrams, is indicated by stable periodic solutions, which occur in response to a limited range of applied currents, denoted by bars along the top axis in Fig. 7*B*. This limited range of currents capable of eliciting tonic behavior is similar to that observed in vitro (Fig. 2*B*). In the bifurcation diagrams in Fig. 7*B*, periodic solutions are shown as thickened branches that vertically straddle, and stretch beyond, the steady-state branch. These periodic branches indicate the maximum and minimum voltage of tonically spiking solutions.

Among model neurons, periodic branches exhibited differences in their stability, their amplitude, and the range of applied currents they spanned. In the early embryo model, there are no stable periodic solutions, representing a neuron that fails to fire tonically to any applied current, like most early embryo neurons recorded in vitro. In contrast, the late embryo model exhibits tonic behavior over a range of ~75 pA. The hatchling model exhibits tonic behavior even more readily, its periodic solutions spanning a range of ~175 pA. This widened range is consistent with our more frequent observations of tonic behavior in hatchling neurons. Additionally, in the late embryo and hatchling models, periodic branches increased in amplitude compared with the early embryo, both by increasing maximum voltage and decreasing minimum voltage (compare to Fig. 3*D* and Fig. 4, *A* and *B*). This is consistent with the experimental finding of increased spike amplitudes over development. Even steady-state solutions changed between model neurons; most notably, as observed in vitro, models representing later developmental stages retained more polarized membrane potentials in response to large applied currents.

Based on these simulations, the three biophysical models display developmental shifts in voltage behavior similar to those observed in current clamp, including an enhanced range of tonic behavior, greater spike amplitude, and a more polarized steady-state voltage.

Developmental changes in conductances selectively extend the range of tonic spiking. We next used the computational model neurons to determine the impact of the conductances that varied over development on the range of tonic spiking in SON neurons (Fig. 8). These simulations start with the hatchling model neuron and then vary g_{HT}, g_{LT}, and g_{Na} one at a time to levels that are present at earlier developmental time points. For each simulation, a bifurcation diagram was constructed, as shown in Fig. 8, *A*, *C*, and *E*, and used to determine

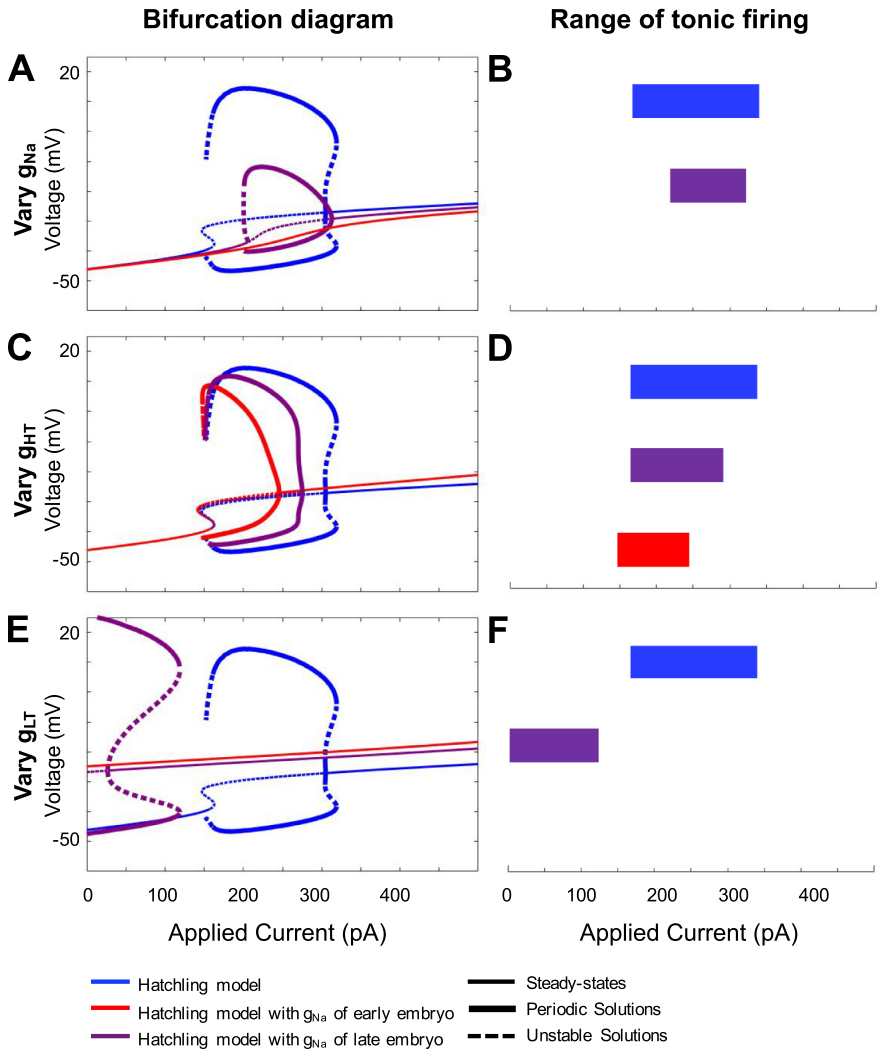

Fig. 8. Current contributions to tonic behavior. *A*, *C*, and *E*: changes to the bifurcation diagrams of the hatchling models when maximal conductances g_{Na}, g_{HT}, and g_{LT} are independently varied to match the average values measured at earlier developmental time points. *B*, *D*, and *F*: decreasing any of the 3 currents decreases the range of applied currents over which the hatchling model displays tonic firing.

the range of applied currents that induce tonic spiking, as shown in Fig. 8, *B*, *D*, and *F*, among other properties, in the model neuron.

Varying g_{Na} primarily affects the amplitude of the tonic spiking solutions. This is clear in Fig. 8*A*, which shows the effect of decreasing g_{Na} in the hatchling model from its initial value of 79.2 nS to embryonic values of 53.5 nS and 33.8 nS. With these decreases, the minimum voltage during tonic spiking becomes less hyperpolarized and the maximum becomes less depolarized, resulting in smaller spikes. With g_{Na} at the level of an early embryo neuron, the periodic branch disappears altogether, so that tonic spiking would not occur for any level of applied current (Fig. 8*B*). In a complementary simulation (not shown) in the model of the early embryo, increasing g_{Na} depolarizes the cell but does not lead to tonic spiking at any level of applied current (the periodic branches that are present are unstable and so would not be observable). Thus a developmental increase in Na^+ conductance is necessary for the production of tonic spiking but not sufficient; a developmental increase in K^+ conductance is also required.

Figure 8*C* shows that decreasing g_{HT} in the hatchling model to embryonic levels has little effect on amplitude but greatly reduces the range of applied currents at which tonic spiking is produced, depolarizes the membrane, and reduces the spike amplitude during tonic spiking. Figure 8*D* shows the decreased range of applied current that produces tonic spiking when g_{HT} is decreased. Thus, by controlling the width of periodic branches, I_{HT} in our models helps control the range of currents that drive tonic behavior. Since a wider range would generally enhance the probability of eliciting tonicity during in vitro current-clamp experiments, the developmental increase in g_{HT} is consistent with our more frequent observation of tonic behavior over development.

The effects of I_{LT} are broadly similar to those of $I_{HT,}$ but because this current is activated at lower voltages its effects on neuronal behavior are more pronounced. In the hatchling, reductions in g_{LT} depolarize the membrane. Because depolarization shifts the periodic branch leftward, tonic behavior emerges at rest, or in response to negative applied currents (Fig. 8, *E* and *F*), conditions that would be unsustainable in a real neuron. These drastic changes suggest that development of I_{LT} is important in countering increases in inward currents and support a balance between developmental increases in I_{LT} and I_{Na} observed experimentally.

DISCUSSION

These experiments illustrate a shift in the physiological phenotype of SON neurons that supports a developmental

increase in excitability. Our examination of active membrane properties revealed concurrent increases in Na^+ and K^+ currents, and the creation of single-compartment model neurons confirmed that these currents may promote excitability.

Although useful in providing a conceptual understanding of how I_{Na}, I_{HT}, and I_{LT} affect neuronal behavior, these biophysical models are not intended to explain every membrane property of actual SON neurons, which undoubtedly exhibit properties unexplored in our simulations. While each biophysical model neuron consists of a single compartment, SON neurons in situ are certainly more compartmentalized, possessing branching fibers that give the cells a multipolar morphology that has been described in the chick at E18–E20 (Yang et al. 1999) and in the adult owl (Carr et al. 1989). How this morphology emerges over development has not been examined but could contribute to the observed developmental changes in SON activity. Also unrepresented in our biophysical model is the effect of ion channel distribution. Immunohistochemical evidence suggests that Na^+ channels cluster on the proximal axons of NM neurons (Kuba and Ohmori 2009) and the subunits supporting I_{HT} are redistributed over development in the membranes of NM and NL neurons (Parameshwaran-Iyer et al. 2003), details that cannot be represented in a single-compartment model. SON neurons also likely express additional ion channel types relative to our biophysical models. One current not considered is the hyperpolarization-activated cation current, I_h. Active over a range of voltages that includes rest and more negative potentials, this inwardly rectifying current, if present in SON, would contribute to our measurements of I_L, resulting in an underestimate of g_L (Robinson and Siegelbaum 2003). While our study focused on currents activated by depolarization, future research could determine whether developmental changes also occur in I_h and other currents.

Even of those currents examined here, it is unlikely that I_{Na}, I_{HT}, and I_{LT} play the same role in every SON neuron as in the model, as diverse conductance values can create similar target behaviors (Marder and Taylor 2011). Nonetheless, the models do demonstrate the impact that the developmental changes in specific channel conductances can have on the timing and shape of action potentials and the range of applied currents that induce tonic spiking, suggesting that increasing I_{Na}, I_{HT}, and I_{LT} is a successful strategy for producing tonic behavior in SON neurons over the developmental time course examined in these experiments.

Effect of temperature. We tested the effect of temperature on voltage behavior with the hatchling model, assuming $Q_{10} = 3$ for τ_n, τ_y, τ_z, and τ_h and $Q_{10} = 1.2$ for g_L, g_{Na}, g_{LT}, and g_{HT} (Sterratt et al. 2011). Increasing temperature from experimental conditions to 40°C had little effect on the range of tonic behavior, although it decreased spike amplitude, confirming physiological relevance of the voltage behavior we observed in vitro.

Role of potassium currents. The developmental increase in I_{Na} we observed is consistent with similar studies in NM (Hong et al. 2016). Potassium currents, in contrast, show some differences from NM in the time course over which they develop and the role they play. The relative absence of I_{HT} in the early embryo is surprising considering its early development in NM and NL (Feng and Morest 2006). Perhaps early I_{HT} is present but resistant to FLX treatment. Alternatively, SON may lag in development compared with lower auditory nuclei. Such a lag has been shown in developing NL compared with NM (Rubel et al. 1976).

At all ages, the K^+ currents we recorded were primarily I_{LT}. This prevalence is surprising given the role of this current in nearby auditory nuclei. In NM, while the dominant K^+ current is I_{HT} (Hong et al. 2016; Rathouz and Trussell 1998), I_{LT} is thought to play an important role in time coding, by lowering input resistance to prevent tonic behavior (Oline et al. 2016). A decrease in tonic behavior in NM results from increasing I_{LT} over development, and a similar effect has been observed in NL (Gao and Lu 2008; Hong et al. 2016). Our biophysical models suggest that I_{LT} plays a different role in SON, promoting tonic behavior by opposing depolarization block. In these model neurons, a developmental increase in I_{Na} promotes tonic spiking only with a concurrent developmental increase in I_{LT} and, to a lesser extent, I_{HT}. Thus the role of a single current varies depending on the broader parameter space, allowing neurons in related nuclei to fulfill distinct roles in the neural circuit.

Time course and cause of developmental changes. Our observations occurred over a time course during which sound stimuli and auditory activity change drastically. While synapses in NM and NL develop by E11 (Jackson et al. 1982), ganglion cells first respond to sound between E15 and E16 (Jones et al. 2006) and thresholds remain high until the embryo breaks into the air space of the egg around E19. Thus the early embryo considered in our work represents the early stages of hearing onset. In addition to sound-driven activity, endogenous activity also occurs in the developing auditory system. Bursting activity in NM and NL is present at E15 and decreases over development, no longer present at E19 (Lippe 1994).

The temporal correlation between changes in ascending excitatory activity and the increased excitability of descending inhibitory neurons suggests that these reciprocally connected areas may influence each other's development. Considering that GABA modulates diverse aspects of development (Ben-Ari et al. 2007) and is capable of inducing plasticity in NM (Carroll and Hyson 2016), SON activity may affect auditory development in NA, NM, and NL. Conversely, emerging auditory input may stimulate SON development. Documentation of experience-dependent plasticity in the avian auditory brain stem, focused on NM and NL, stretches back to classic experiments by Levi-Montalcini, showing abnormal development following otocyst removal (Levi-Montalcini 1949). Deafness-induced plasticity persists into maturity and includes changes in ion channel expression. For instance, within NM expression of $K_v3.1$ and $K_v1.1$ subunits, which support I_{HT} and I_{LT}, decreases within 3 h of deafness (Lu et al. 2004). Although the specific signal involved in this downregulation has not been identified, individual neurons have been demonstrated to upregulate currents rapidly in response to depolarization as in the stomatogastric ganglion of the crab (Golowasch et al. 1999). If auditory input similarly regulates currents in SON, emerging auditory input could increase the expression of these currents during development.

Alternatively, the observed changes in SON may be driven not by emerging activity but by developmental regulation of gene expression. Similar developmental increases in channel expression have been demonstrated in the chick auditory brain stem through electrophysiology (Gao and Lu 2008; Hong et al.

2016) and immunohistochemistry (Feng and Morest 2006). In NM and NL, different channel subunits have even been shown to be regulated by different mechanisms. Developmental increases in $K_v3.1$ occur with synapse formation in cultured chick brain stem neurons, but increases in $K_v1.1$ require other signals present in vivo (Feng and Morest 2001). Thus it is likely that changes in SON similarly include both activity-dependent and activity-independent aspects.

Functional implications of developmental changes. A remaining question is how changes in SON accommodate the developing auditory system. Our recordings indicate that SON neurons require more current to generate action potentials in early embryos than in hatchlings. This adds support to the hypotheses proposed by Lippe (1994) following his observations of rhythmic bursting activity in NM and NL of embryos. The higher rheobase in embryonic neurons suggests that they would work as a type of high-pass filter with regard to synaptic drive and fire only in response to a burst of embryonic activity that activates multiple synapses synchronously. Lippe (1994) suggested that this filtering in the auditory system might serve to help set up and stabilize innervation patterns that support tonotopic organization. Thus the less excitable phenotype observed at early time points may facilitate normal auditory development.

Limiting inhibitory activity early in development may also serve a protective function. Inhibition in the absence of auditory nerve activity has been shown to disrupt ribosomes in one target of SON, NM (Carroll and Hyson 2016). These changes imply a corresponding disruption of protein synthesis and are an early indicator of cell death in NM neurons. Thus limiting SON activity before hearing onset could serve to preserve the developing sensory circuit.

In contrast, the emerging excitability of SON neurons following hearing onset likely reflects matured auditory processing. Consistent with the proposed role of SON in controlling gain in NA, NM, and NL, increased SON activity following hearing onset could scale up inhibition to parallel increased excitation by the auditory nerve. Changing ion channel expression to promote increased spiking is one mechanism by which this scaling might occur. Consistent with this theory of emerging inhibition is the developmental time course over which GABA terminals increase in NM and NL (E14–E18) (Korn et al. 2012) and GABA becomes inhibitory in NM through increased expression of I_{LT} (E14–E18) (Howard et al. 2007).

Changes in activity patterns may also represent the mature system's need for variation in physiological phenotype across the SON population. One such need might arise developmentally if exposure to a more diverse range of sound frequencies demands more diversity in the SON population, relating to its own topographic mapping (Tabor et al. 2012) or that of its targets. Indeed, inhibition has been proposed to play distinct roles in different frequency regions of the target NL (Tang and Lu 2012). These authors found that, compared with those in low-frequency neurons in NL, evoked inhibitory postsynaptic potentials in mid- and high-frequency neurons are slower with decay times more dependent on stimulus frequency, suggesting a distinction between inhibitory mechanisms at the synaptic level. Also in contrast to low-frequency regions, these mid- to high-frequency NL neurons also receive ambiently released GABA that emerges over auditory development (Tang et al. 2011). Nishino et al. (2008) linked these tonotopic distinctions to inhibition specifically from SON by showing in vivo that only low-frequency NL neurons exhibit level-dependent suppression through SON activity. Interestingly, SON neurons phase-lock to lower-frequency stimuli but not to frequencies above 2 kHz, consistent with distinct roles for inhibition depending on stimulus pitch (Coleman et al. 2011). Future experiments could explore whether enhanced tonic behavior in SON might represent an emerging need for the processing of high-frequency sounds by examining whether observations of tonic vs. nontonic behavior correspond with SON topography.

Because we recorded from a limited range of applied currents, it is not clear from our experiments whether SON can be clearly divided into two populations of tonic and nontonic. In vitro heterogeneity could help explain the heterogeneity observed structurally (Carr et al. 1989; Lachica et al. 1994) and physiologically in vivo (Coleman et al. 2011; Tabor et al. 2012). However, our simulations show that small variations in conductance parameters can disrupt or produce tonic behavior. Such changes in maximal conductance can occur over short periods (Golowasch et al. 1999). Thus an alternative hypothesis, to be examined in future experiments, is that the ability to act tonically can be recruited in the SON population based on auditory input in the present environment. This flexibility may persist in inhibitory feedback circuits even beyond the auditory system.

While it is widely accepted that inhibition plays a role in shaping the output of excitatory neural circuits, data from immature subjects are often integrated into theories of how these circuits process information (for instance, Funabiki et al. 1998), with the tacit assumption that inhibitory neurons are uniform and consistent even as excitatory connections are modified by age or experience. Our experiments challenge this assumption, as they suggest that the physiological properties of inhibitory neurons are not stable across development but become more excitable as the bird transitions from embryo to hatchling. This developmental change in the intrinsic properties of inhibitory neurons has functional consequences for the coding of acoustic information, by enhancing the availability of inhibitory modulation of excitatory drive. The developmental delay in this enhanced availability of inhibition may be adaptive in corresponding with the presumptive increase in excitatory drive as the bird becomes exposed to airborne sounds.

ACKNOWLEDGMENTS

We are grateful to Dr. R. M. Burger for review of and comments on a draft of this manuscript and to Dr. C. Schatschneider for assistance with statistical modeling.

GRANTS

This work was partially supported by the Florida State University Research Foundation R. Bruce Masterton Endowment (R. L. Hyson) and National Science Foundation Grant IOS-1656360.

DISCLOSURES

No conflicts of interest, financial or otherwise, are declared by the authors.

AUTHOR CONTRIBUTIONS

B.J.C., R.B., and R.L.H. conceived and designed research; B.J.C. performed experiments; B.J.C. analyzed data; B.J.C., R.B., and R.L.H. interpreted results of experiments; B.J.C. prepared figures; B.J.C. drafted manuscript;

B.J.C., R.B., and R.L.H. edited and revised manuscript; B.J.C., R.B., and R.L.H. approved final version of manuscript.

REFERENCES

Anwar H, Li X, Bucher D, Nadim F. Functional roles of short-term synaptic plasticity with an emphasis on inhibition. *Curr Opin Neurobiol* 43: 71–78, 2017. doi:10.1016/j.conb.2017.01.002.

Armstrong CM, Gilly WF. Access resistance and space clamp problems associated with whole-cell patch clamping. *Methods Enzymol* 207: 100–122, 1992. doi:10.1016/0076-6879(92)07007-B.

Auerbach BD, Rodrigues PV, Salvi RJ. Central gain control in tinnitus and hyperacusis. *Front Neurol* 5: 206, 2014. doi:10.3389/fneur.2014.00206.

Bar-Yehuda D, Korngreen A. Space-clamp problems when voltage clamping neurons expressing voltage-gated conductances. *J Neurophysiol* 99: 1127–1136, 2008. doi:10.1152/jn.01232.2007.

Ben-Ari Y, Gaiarsa JL, Tyzio R, Khazipov R. GABA: a pioneer transmitter that excites immature neurons and generates primitive oscillations. *Physiol Rev* 87: 1215–1284, 2007. doi:10.1152/physrev.00017.2006.

Burger RM, Cramer KS, Pfeiffer JD, Rubel EW. Avian superior olivary nucleus provides divergent inhibitory input to parallel auditory pathways. *J Comp Neurol* 481: 6–18, 2005. doi:10.1002/cne.20334.

Carr CE, Fujita I, Konishi M. Distribution of GABAergic neurons and terminals in the auditory system of the barn owl. *J Comp Neurol* 286: 190–207, 1989. doi:10.1002/cne.902860205.

Carroll BJ, Hyson RL. A role for inhibition in deafness-induced plasticity of the avian auditory brainstem. *Neuroscience* 327: 10–19, 2016. doi:10.1016/j.neuroscience.2016.04.015.

Coleman WL, Fischl MJ, Weimann SR, Burger RM. GABAergic and glycinergic inhibition modulate monaural auditory response properties in the avian superior olivary nucleus. *J Neurophysiol* 105: 2405–2420, 2011. doi:10.1152/jn.01088.2010.

Daou A, Ross MT, Johnson F, Hyson RL, Bertram R. Electrophysiological characterization and computational models of HVC neurons in the zebra finch. *J Neurophysiol* 110: 1227–1245, 2013. doi:10.1152/jn.00162.2013.

Feng J, Morest DK. Developmental expression of a voltage-dependent potassium channel (Kv3.1) in auditory neurons without cochlear input. *J Neurosci Res* 65: 121–128, 2001. doi:10.1002/jnr.1135.

Feng JJ, Morest DK. Development of synapses and expression of a voltage-gated potassium channel in chick embryonic auditory nuclei. *Hear Res* 216-217: 116–126, 2006. doi:10.1016/j.heares.2006.01.012.

Fukui I, Burger RM, Ohmori H, Rubel EW. GABAergic inhibition sharpens the frequency tuning and enhances phase locking in chicken nucleus magnocellularis neurons. *J Neurosci* 30: 12075–12083, 2010. doi:10.1523/JNEUROSCI.1484-10.2010.

Funabiki K, Koyano K, Ohmori H. The role of GABAergic inputs for coincidence detection in the neurones of nucleus laminaris of the chick. *J Physiol* 508: 851–869, 1998. doi:10.1111/j.1469-7793.1998.851bp.x.

Galicia S, Cortes C, Cebada J, Méndez-Balbuena I, Flores A. Firing properties of auditory primary afferents from the basilar papilla in the chick. *Int J Dev Neurosci* 44: 92–101, 2015. doi:10.1016/j.ijdevneu.2015.05.007.

Gao H, Lu Y. Early development of intrinsic and synaptic properties of chicken nucleus laminaris neurons. *Neuroscience* 153: 131–143, 2008. doi:10.1016/j.neuroscience.2008.01.059.

Golowasch J, Abbott LF, Marder E. Activity-dependent regulation of potassium currents in an identified neuron of the stomatogastric ganglion of the crab *Cancer borealis*. *J Neurosci* 19: RC33, 1999.

Hong H, Rollman L, Feinstein B, Sanchez JT. Developmental profile of ion channel specializations in the avian nucleus magnocellularis. *Front Cell Neurosci* 10: 80, 2016. doi:10.3389/fncel.2016.00080.

Howard MA, Burger RM, Rubel EW. A developmental switch to GABAergic inhibition dependent on increases in Kv1-type K^+ currents. *J Neurosci* 27: 2112–2123, 2007. doi:10.1523/JNEUROSCI.5266-06.2007.

Jackson H, Hackett JT, Rubel EW. Organization and development of brain stem auditory nuclei in the chick: ontogeny of postsynaptic responses. *J Comp Neurol* 210: 80–86, 1982. doi:10.1002/cne.902100109.

Jones TA, Jones SM, Paggett KC. Emergence of hearing in the chicken embryo. *J Neurophysiol* 96: 128–141, 2006. doi:10.1152/jn.00599.2005.

Korn MJ, Koppel SJ, Li LH, Mehta D, Mehta SB, Seidl AH, Cramer KS. Astrocyte-secreted factors modulate the developmental distribution of inhibitory synapses in nucleus laminaris of the avian auditory brainstem. *J Comp Neurol* 520: 1262–1277, 2012. doi:10.1002/cne.22786.

Kuba H, Koyano K, Ohmori H. Development of membrane conductance improves coincidence detection in the nucleus laminaris of the chicken. *J Physiol* 540: 529–542, 2002. doi:10.1113/jphysiol.2001.013365.

Kuba H, Ohmori H. Roles of axonal sodium channels in precise auditory time coding at nucleus magnocellularis of the chick. *J Physiol* 587: 87–100, 2009. doi:10.1113/jphysiol.2008.162651.

Lachica EA, Rübsamen R, Rubel EW. GABAergic terminals in nucleus magnocellularis and laminaris originate from the superior olivary nucleus. *J Comp Neurol* 348: 403–418, 1994. doi:10.1002/cne.903480307.

Levi-Montalcini R. The development to the acoustico-vestibular centers in the chick embryo in the absence of the afferent root fibers and of descending fiber tracts. *J Comp Neurol* 91: 209–241, 1949. doi:10.1002/cne.900910204.

Lippe WR. Rhythmic spontaneous activity in the developing avian auditory system. *J Neurosci* 14: 1486–1495, 1994.

Lu Y, Monsivais P, Tempel BL, Rubel EW. Activity-dependent regulation of the potassium channel subunits Kv1.1 and Kv3.1. *J Comp Neurol* 470: 93–106, 2004. doi:10.1002/cne.11037.

MacLeod KM, Carr CE. Beyond timing in the auditory brainstem: intensity coding in the avian cochlear nucleus angularis. *Prog Brain Res* 165: 123–133, 2007. doi:10.1016/S0079-6123(06)65008-5.

Marder E, Taylor AL. Multiple models to capture the variability in biological neurons and networks. *Nat Neurosci* 14: 133–138, 2011. doi:10.1038/nn.2735.

Mozzachiodi R, Byrne JH. More than synaptic plasticity: role of nonsynaptic plasticity in learning and memory. *Trends Neurosci* 33: 17–26, 2010. doi:10.1016/j.tins.2009.10.001.

Nishino E, Yamada R, Kuba H, Hioki H, Furuta T, Kaneko T, Ohmori H. Sound-intensity-dependent compensation for the small interaural time difference cue for sound source localization. *J Neurosci* 28: 7153–7164, 2008. doi:10.1523/JNEUROSCI.4398-07.2008.

Oh MM, Disterhoft JF. Increased excitability of both principal neurons and interneurons during associative learning. *Neuroscientist* 21: 372–384, 2015. doi:10.1177/1073858414537382.

Oline SN, Ashida G, Burger RM. Tonotopic optimization for temporal processing in the cochlear nucleus. *J Neurosci* 36: 8500–8515, 2016. doi:10.1523/JNEUROSCI.4449-15.2016.

Parameshwaran-Iyer S, Carr CE, Perney TM. Localization of KCNC1 (Kv3.1) potassium channel subunits in the avian auditory nucleus magnocellularis and nucleus laminaris during development. *J Neurobiol* 55: 165–178, 2003. doi:10.1002/neu.10198.

Puelles L, Martinez-de-la-Torre M, Paxinos G, Watson C, Martinez S. *The Chick Brain in Stereotaxic Coordinates: An Atlas Featuring Neuromeric Subdivisions and Mammalian Homologies* (1st ed.). Amsterdam: Academic, 2007.

Rathouz M, Trussell L. Characterization of outward currents in neurons of the avian nucleus magnocellularis. *J Neurophysiol* 80: 2824–2835, 1998. doi:10.1152/jn.1998.80.6.2824.

Richardson BD, Brozoski TJ, Ling LL, Caspary DM. Targeting inhibitory neurotransmission in tinnitus. *Brain Res* 1485: 77–87, 2012. doi:10.1016/j.brainres.2012.02.014.

Robinson RB, Siegelbaum SA. Hyperpolarization-activated cation currents: from molecules to physiological function. *Annu Rev Physiol* 65: 453–480, 2003. doi:10.1146/annurev.physiol.65.092101.142734.

Rothman JS, Manis PB. The roles potassium currents play in regulating the electrical activity of ventral cochlear nucleus neurons. *J Neurophysiol* 89: 3097–3113, 2003. doi:10.1152/jn.00127.2002.

Rubel EW, Smith DJ, Miller LC. Organization and development of brain stem auditory nuclei of the chicken: ontogeny of n. magnocellularis and n. laminaris. *J Comp Neurol* 166: 469–489, 1976. doi:10.1002/cne.901660408.

Scott LL, Mathews PJ, Golding NL. Posthearing developmental refinement of temporal processing in principal neurons of the medial superior olive. *J Neurosci* 25: 7887–7895, 2005. doi:10.1523/JNEUROSCI.1016-05.2005.

Sterratt D, Graham B, Gillies A, Willshaw D. *Principles of Computational Modelling in Neuroscience*. Cambridge, UK: Cambridge Univ. Press, 2011. doi:10.1017/CBO9780511975899.

Sullivan WE, Konishi M. Segregation of stimulus phase and intensity coding in the cochlear nucleus of the barn owl. *J Neurosci* 4: 1787–1799, 1984.

Sung MJ, Ahn HS, Hahn SJ, Choi BH. Open channel block of Kv3.1 currents by fluoxetine. *J Pharmacol Sci* 106: 38–45, 2008. doi:10.1254/jphs.FP0070759.

Tabor KM, Coleman WL, Rubel EW, Burger RM. Tonotopic organization of the superior olivary nucleus in the chicken auditory brainstem. *J Comp Neurol* 520: 1493–1508, 2012. doi:10.1002/cne.22807.

Takahashi T, Moiseff A, Konishi M. Time and intensity cues are processed independently in the auditory system of the owl. *J Neurosci* 4: 1781–1786, 1984.

Tang ZQ, Dinh EH, Shi W, Lu Y. Ambient GABA-activated tonic inhibition sharpens auditory coincidence detection via a depolarizing shunting mechanism. *J Neurosci* 31: 6121–6131, 2011. doi:10.1523/JNEUROSCI.4733-10.2011.

Tang ZQ, Lu Y. Two $GABA_A$ responses with distinct kinetics in a sound localization circuit. *J Physiol* 590: 3787–3805, 2012. doi:10.1113/jphysiol.2012.230136.

Willmore BD, Cooke JE, King AJ. Hearing in noisy environments: noise invariance and contrast gain control. *J Physiol* 592: 3371–3381, 2014. doi:10.1113/jphysiol.2014.274886.

Yang L, Monsivais P, Rubel EW. The superior olivary nucleus and its influence on nucleus laminaris: a source of inhibitory feedback for coincidence detection in the avian auditory brainstem. *J Neurosci* 19: 2313–2325, 1999.